

Observation of Coherent Reaction Dynamics in Heme Proteins

Leyun Zhu, J. Timothy Sage, Paul M. Champion*

Femtosecond laser pulses, resonant with the Soret band of the nitric oxide complex of myoglobin (MbNO), were used to probe coherent, low-frequency nuclear motion of the heme group after photolysis. Distinct oscillations with periods of 430 and 150 femtoseconds were observed and are attributed to heme doming and iron-histidine motion, respectively. These results verify that the nuclear motion of the heme is strongly coupled to the ligand binding reaction and demonstrate that such motion is not determined by overdamped (diffusive) dynamics. The relative phases and frequencies of the nuclear motion of the photoproduct suggest that the coherence arises from impulsive electronic forces associated with the spin-state change of the heme iron atom and the depopulation of its d_{z^2} orbital during the bond-breaking event.

Heme proteins play a crucial role in numerous biological reactions. In this report, we focus on the elementary electronic and nuclear events associated with diatomic ligand binding and dissociation in myoglobin (Mb). Femtosecond coherence spectroscopy (1), which has only recently been applied to biological systems (2, 3), is used to probe the low-frequency nuclear motion of the heme group, subsequent to the photolysis of nitric oxide from the ligated protein (denoted as MbL or MbNO). The experiments (4) probe coherent nuclear motion induced by the forces that develop in response to the rapid electronic rearrangements taking place during ligand photolysis. This motion involves the nuclear coordinates that are most strongly coupled to the reaction, and, as such, these experiments reveal contributions to the "reaction coordinate" that are directly associated with the heme group. For example, we observe a robust, low-frequency oscillation near 2.3 THz (75 cm^{-1}) that is assigned to the heme doming motion (ν_{dome}), a coordinate believed to be important for the quantitative understanding of the ligand binding reaction and the optical properties of the heme (5). In addition to heme doming, we observe a strong oscillation of the covalent iron-histidine linkage ($\nu_{\text{Fe-His}}$) at 6.6 THz (220 cm^{-1}).

Earlier time-resolved resonance Raman studies (6) have probed a transient photoproduct population (Mb*) that is created upon ligand photolysis. Such studies use relatively high-energy laser pulses (~ 1 to 10 mJ), and three photons are involved in the preparation-interrogation process (7). In contrast to the "reaction-specific" modes selected by the femtosecond coherence experiments reported here, the time-resolved resonance Raman studies probe only those modes coupled to the resonant absorption

bands of Mb* and have not directly revealed the low-frequency heme doming motion.

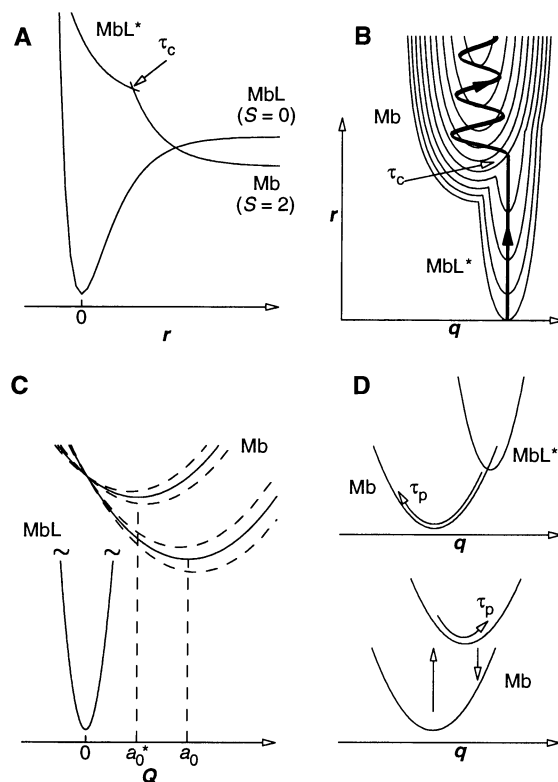
The observation of heme doming and iron-histidine coherence, subsequent to the photolysis of MbNO, demonstrates that models based on diffusive (8) or dispersive (9) transport do not adequately describe the subangstrom motion of functionally important degrees of freedom of the heme. These results strongly suggest the need for models that treat the heme group quantum mechanically (10) yet "dress" it with the sur-

rounding larger-scale protein motion, which is more properly described by classical diffusive or dispersive transport.

We sketch in Fig. 1 views of the potential energy surfaces along three of the key nuclear coordinates. When a ligand is bound to the heme (MbL), the six d electrons usually pair up to form a spin singlet ($S = 0$) state (for a spin-triplet iron ground state, which may be a better approximation for NO ligation, simply replace $S = 0$ by $S = 1$ in Fig. 1). As the Fe-L distance, r , increases from its equilibrium value ($r = 0$ in Fig. 1A), the iron undergoes electronic rearrangement to form a spin quintet ($S = 2$), corresponding to the ground state of the deligated heme (Mb). Thus, the coordinate r can be viewed as the traditional "reaction coordinate." The intersecting curves above $r = 0$ in Fig. 1A represent an oversimplified picture of the optically accessible excited state, MbL*, and of its mixing with the intervening charge-transfer or d electron excited states (11) that evidently facilitates the rapid intersystem crossing to the spin-forbidden $S = 2$ level.

However, as pointed out by Agmon and Hopfield (12), the heme ligation reaction is more complicated than indicated by the potential surface of Fig. 1A. Other functionally important coordinates can coexist along axes that are "perpendicular" to the

Fig. 1. A simplified representation of the multidimensional potential energy surface for ligand binding to and dissociation from the heme of myoglobin (Mb). (A) A cut along the Fe-L coordinate (r). (B) A two-dimensional contour plot of the excited-state (MbL*) and ground-state (Mb) potential surfaces and the nuclear motion subsequent to photoexcitation. In principle, the coordinate q can represent any mode coupled to the reaction, but here it is taken as the Fe-His mode (the absence of Raman activity in the Fe-His mode of MbNO indicates that it is not displaced upon photoexcitation). (C) A ground-state cut along the heme doming coordinate, Q , where the dashed curves represent changes in the equilibrium position induced by rapid protein fluctuations. The slower evolution of the equilibrium position, $\langle a(t) \rangle$, as a result of relaxation of the protein material is shown both at early times (a_0^*) and at equilibrium (a_0). (D) The upper curves show the development of coherent nuclear motion along the displaced Fe-His coordinate of Mb at $t = \tau_c$, when the system crosses into the ground electronic state along r . The lower curves depict the preparation of a ground-state vibrational (Raman) coherence along the Fe-His mode of Mb brought about by resonant excitation of a shifted (Franck-Condon active) electronic-state surface. The coherence signals associated with the upper and lower pairs of curves in (D) should be nearly π out of phase, if the laser pulse width (τ_p) is much longer than τ_c and is one-half the oscillatory period.



Department of Physics, Northeastern University, Boston, MA 02115, USA.

*To whom correspondence should be addressed.

coordinate r . For example, Fig. 1B depicts a two-dimensional potential surface involving both the optically prepared initial electronic state, MbL^* , and the fully dissociated electronic state, Mb . The evolution of the optically prepared nuclear wave packet is strongly perturbed at time $t = \tau_c$, during the barrierless electronic transition from MbL^* to Mb , because it encounters a new potential surface that is displaced along q . The forces associated with this displacement lead to damped oscillatory motion of the product-state mode as shown by the thick solid line. The long lifetime of the electronic ground state allows observation of the product-state vibrational coherences.

In Fig. 1C we show a harmonic approximation to the ground-state potentials of a significantly displaced ($\sim 0.45 \text{ \AA}$) product-state mode, Q , describing heme doming. The dashed curves indicate the possibility of dynamic changes in the equilibrium positions, induced by rapid conformational fluctuations of the globular protein material (5). The quantity a_0 represents the mean value of the equilibrium position when the protein is completely relaxed. Similarly, a_0^* represents the mean value at some early time subsequent to photolysis or at low temperature when the protein coordinates are "frozen" and not completely free to relax. However, within a simple linear harmonic cross-coupling model (5), the curvature of the potential remains fixed and the oscillations corresponding to heme doming are unaffected as the protein relaxes (13).

Figure 1D presents a view along the Fe-His coordinate, which is also coupled to the dissociation reaction. The upper pair of potentials is a cut of Fig. 1B at τ_c . The crossing to the ground-state surface evidently occurs very rapidly along r ($\tau_c \ll 75 \text{ fs}$), and the net loss of electron density in the antibonding d_{z^2} orbital leads to a contraction of the Fe-His bond during the laser pulse (14). Thus, the product-state wave packet propagates to the left during the duration of the pump pulse, and a phase shift of $\sim \pi$ is expected (15) to appear when the reaction-driven coherence of the photoproduct species is compared to a ground-state photon-driven vibrational coherence of Mb . The lower pair of potentials in Fig. 1D depicts the preparation of such a ground-state Raman coherence by the electric field interventions of a laser pump pulse. The bra (or ket) wave packet propagates during the pulse (τ_p) so that the nonstationary wave packet created after the second electric field intervention (short downward arrow) leads to a maximum absorbance (zero phase shift) when probing is done at wavelengths to the red of the absorption maximum (to the right of the long arrow). When probing is done to the blue (to the left of the long arrow), the absorbance is maximized after

about one-half of the vibrational cycle, so that a relative phase shift of $\sim \pi$ should appear in the time-dependent signals relative to those probed in the red.

To illustrate the differences between the Mb and the photolyzed MbNO samples, we display in Figs. 2 and 3 some representative time-domain signals at various pump and probe wavelengths. Figure 2A shows the absorption spectra of the two samples along with the pump-pulse spectral envelope (dashed line). The diamond near 429 nm represents the isosbestic point between MbNO and its photoproduct (Mb), whereas the analogous point near 440 nm corresponds to the isosbestic point between the ground and excited states of Mb . If we probe close to these wavelengths (Fig. 3), the signals associated with the differential absorption of the ground- and excited-state populations are diminished and the oscillatory components, due to coherent nuclear motion, are enhanced. However, in Fig. 2B we have detuned slightly to the red of the 429-nm isosbestic point so that the anti-bleach of MbNO (change in transmittance, $\Delta T < 0$) can be contrasted with the bleach ($\Delta T > 0$) of Mb . Thus, the signals we associate with the MbNO sample do not arise from a residual population of Mb , which has not rebound the ligand between the laser pulse pairs. More importantly, the samples display out-of-phase oscillatory sig-

nals with periods of 150 fs that correspond to the 220-cm^{-1} Fe-His mode of Mb . [MbNO does not have a resonance Raman-active mode associated with the Fe-His motion; the closest Raman-active vibration is due to pyrrole tilting (16) at 255 cm^{-1} .]

The signals in Fig. 3 show the relative phase relations more clearly. The lower two panels in Fig. 3 depict the experiments on Mb , and the phases of the oscillatory absorbance signals (corresponding to $-\Delta T$), determined (17) by linear predictive singular value decomposition (LPSVD), are plotted in the inset (the circles and the squares are for $\nu_{\text{Fe-His}}$ and ν_{doming} , respectively). We can refer to the lower part of Fig. 1D to see that the phase associated with the Mb absorbance signal ($-\Delta T$) should occur near zero when probed in the red and near π when probed in the blue. Although the absolute phases are not in perfect agreement (nor should they be) with the simple picture given in Fig. 1D, the general trend is correct. Both the Fe-His and the doming modes show a phase shift of $\sim \pi$ as the monochromator probe wavelength, λ_m , is tuned from red (solid symbols) to blue (open symbols).

The signals and relative phases associated with the photolyzed MbNO sample are found in the upper two panels of Fig. 3. For the Fe-His mode, the phases are shifted by $\sim \pi$ with respect to the Mb signals shown in

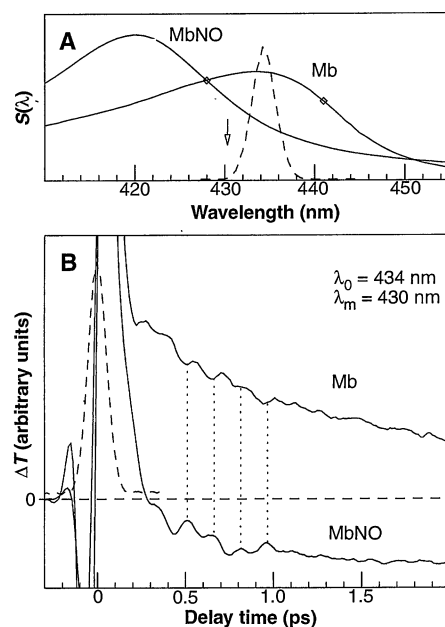


Fig. 2. (A) The optical absorption spectra of Mb and MbNO along with the laser pulse envelope (dashed curve with center wavelength of λ_0) and the detection wavelength (arrow, λ_m) used in obtaining the signals shown in (B), which depicts the change in the transmittance (ΔT) as a function of probe pulse delay when Mb and MbNO are used as starting material. The dashed line is the auto-correlation trace of the laser pulse.

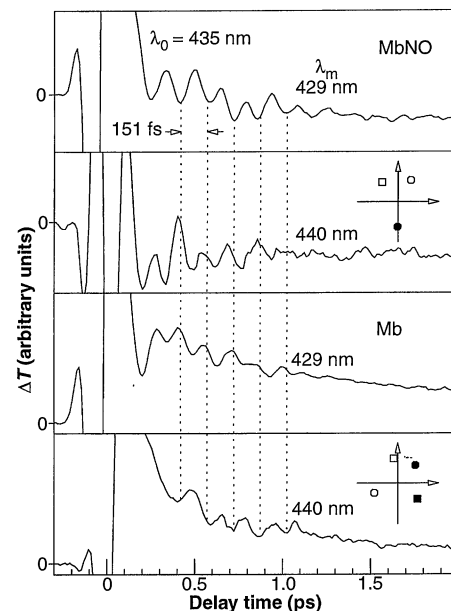


Fig. 3. A more detailed study of the relative phase of the signals as a function of sample state and probe wavelength, λ_m . The symbols are a polar plot of the phases extracted from the data by the LPSVD fitting procedure. The circles and squares represent the Fe-His and heme doming modes, respectively. The solid (open) symbols correspond to probe wavelengths in the red (blue). The phase of the low-frequency mode in the MbNO sample could not be reliably extracted at 440 nm.

the lower panels. This shift occurs because the 75-fs pulse width is just one-half the oscillatory period of the Fe–His mode, and the impulsive forces are acting in opposite directions over the duration of the pulse (Fig. 1D). On the other hand, the low-frequency doming oscillation has a period (430 fs) that is much longer than the pulse width, and its relative phase shift is much smaller when the two samples are compared at 429 nm (open squares).

In Fig. 4 we present a more detailed analysis of the oscillatory signals associated with the MbNO sample. Traces a and b show the raw data and the LPSVD fitting function, respectively, whereas trace d is the oscillatory component arising from the Fe–His vibration at 220 cm^{-1} . Trace c is the residual of the raw data, after the component in trace d has been subtracted. It shows a robust oscillation with a period (430 fs) that we assign to the doming motion of the heme photoproduct state. The power spectrum derived from the LPSVD analysis is given in trace e, where it can be compared to the continuous wave (cw) resonance Raman spectra of Mb (trace f) and MbNO (trace g) taken in stationary sample cells with the same average power (10 mW) as in the femtosecond coherence experiments. The presence of the mode at 220 cm^{-1} in the power spectrum provides definitive evidence that the time-domain experiment probes the coherent mo-

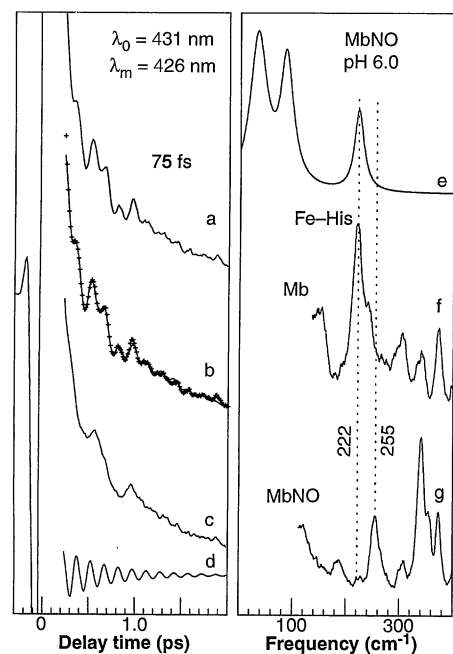


Fig. 4. The oscillatory data (curve a) and the LPSVD fit (curve b) for MbNO. The residual showing the heme doming mode (curve c) is obtained by subtraction of the 220-cm^{-1} oscillatory component (curve d). The power spectrum from curve b is shown in curve e so that it can be compared with the cw resonance Raman spectra of Mb (curve f) and MbNO (curve g).

tion of the heme reaction product rather than a ground-state impulsive scattering process associated with MbNO.

The reason that the ground-state scattering of MbNO is difficult to observe in the present experiments can be traced to the rapid inter-system crossing that takes place at τ_c in Fig. 1A. If the crossing occurs in $\ll 75$ fs as suggested by the relative phase shift of the Fe–His oscillations (15), spin selection rules will greatly diminish the electric dipole coupling between the MbNO excited and ground-state surfaces when $t \geq \tau_c$. This effect reduces the strength of the ground-state coherence signals because the propagation time on the excited-state surface becomes limited by τ_c , with correspondingly small coordinate displacements on the ground-state surface. In contrast, the propagation time is less important for coherences prepared directly on a displaced excited-state (or product-state) surface. However, the coherences of MbNO* are damped much too rapidly by electronic population decay to be observed.

The assignment of the low-frequency oscillation observed near 75 cm^{-1} to the doming motion of the heme is consistent with predictions based on analysis of the optical spectra and the ligand binding kinetics (5) as well as with recent normal-mode calculations (18). The dephasing time (≥ 0.5 ps) associated with the doming oscillation is typical for vibrational modes of the heme, as estimated from their Raman linewidths. This result emphasizes the need for models (10) that incorporate a fully quantum mechanical description of the heme doming motion and shows that such motion is not overdamped and rendered diffusive by the protein, as recently implied (8). The simple linear cross-coupling model (5, 10) used previously to describe the Mb ligand binding kinetics and optical absorption spectra appears to work well in the current context. At this level of analysis, the oscillation frequency of the heme doming mode is independent of time, and only the linear coupling and equilibrium position of the potential well are changing as the protein relaxes on slower time scales (see Fig. 1C).

In summary, the relative phases of the coherence signals and their dependence on the initial sample state (Mb versus MbNO) and the period of the oscillation being examined suggest that photolysis takes place promptly ($\tau_c \ll 75$ fs) and is followed by rapid Fe–His compression ($T/4 = 37$ fs, where T is the period) and heme doming ($T/4 = 107$ fs). These experiments demonstrate that the technique of femtosecond coherence spectroscopy has the capability to select out and identify important low-frequency “reactive” modes in complex biological systems and that such modes are not necessarily overdamped.

REFERENCES AND NOTES

1. M. J. Rosker *et al.*, *Phys. Rev. Lett.* **57**, 321 (1986); S. Ruhman *et al.*, *J. Chem. Phys.* **86**, 6563 (1987); A. H. Zewail, *Science* **242**, 1645 (1988); H. L. Fragnito *et al.*, *Chem. Phys. Lett.* **160**, 101 (1989); N. F. Scherer *et al.*, *J. Chem. Phys.* **96**, 5544 (1992); W. T. Pollard and R. A. Mathies, *Annu. Rev. Phys. Chem.* **43**, 497 (1992); L. Dhar *et al.*, *Chem. Rev.* **94**, 157 (1994).
2. S. L. Dexheimer *et al.*, *Chem. Phys. Lett.* **188**, 61 (1992); M. Vos *et al.*, *Nature* **363**, 320 (1993).
3. L. Zhu *et al.*, *Phys. Rev. Lett.* **72**, 301 (1994).
4. In the experiments reported here we used sequential perpendicularly polarized 75-fs pump and probe pulses (having a central wavelength, λ_0 , and a width, $\Delta\lambda$, ~ 5 to 10 nm), which traverse the sperm whale Mb samples in a near parallel geometry. To detect the probe pulse with wavelength specificity (λ_m), we used a monochromator to filter the signal before detection by a photomultiplier. More details of the experimental setup and the detection scheme for monitoring the pump-induced changes in the sample transmittance can be found elsewhere (3). The NO ligand was chosen for the photolysis experiments because its “reset” time, which is controlled by picosecond geminate recombination, is much faster than the 76-MHz laser repetition rate. The samples were also studied as a function of pH, and no differences were detected for samples prepared in a 0.2 M borate buffer at pH 8.5 (Fig. 3) or in a 0.1 M phosphate buffer at pH 6.0 (Figs. 2 and 4).
5. V. Šrajer *et al.*, *Phys. Rev. Lett.* **57**, 1267 (1986); V. Šrajer *et al.*, *J. Am. Chem. Soc.* **110**, 6656 (1988); V. Šrajer and P. M. Champion, *Biochemistry* **30**, 7390 (1991); P. M. Champion, *J. Raman Spectrosc.* **23**, 557 (1992).
6. D. L. Rousseau and J. M. Friedman, in *Biological Applications of Raman Spectroscopy*, T. G. Spiro, Ed. (Wiley, New York, 1988), vol. 3, pp. 133–215; E. Findsen, T. Scott, M. Chance, J. Friedman, M. Ondrias, *J. Am. Chem. Soc.* **107**, 3355 (1985).
7. The three photons (six electric field interventions) associated with the time-resolved Raman experiments are better classified within a χ^5 nonlinear susceptibility framework. On the other hand, the low-laser pulse energy (100-pJ) experiments reported here photolyze only $\sim 1\%$ of the MbNO sample (on the assumption of a quantum yield of unity) yet give rise to signals comparable to those found in pure Mb samples. This observation requires a two-photon description (four electric field interventions) and is classified within a χ^3 nonlinear susceptibility framework. See D. Lee and A. C. Albrecht, in *Advances in Infrared and Raman Spectroscopy*, R. Clark and R. Hester, Eds. (Wiley, New York, 1985), vol. 12, pp. 179–213, or S. Mukamel, *Annu. Rev. Phys. Chem.* **41**, 647 (1990), for general discussions of the nonlinear susceptibility classification schemes. Other cases of product-state coherence at the χ^3 level have been reported in small molecules. See, for example, M. Rosker *et al.*, *J. Chem. Phys.* **89**, 6113 (1988); U. Banin *et al.*, *ibid.* **98**, 4391 (1993); N. Pugliano *et al.*, *ibid.* **99**, 7273 (1993).
8. N. Agmon and S. Rabinovich, *J. Chem. Phys.* **97**, 7270 (1992).
9. Y. Berlin, N. Chekunaev, V. I. Goldanskii, *Chem. Phys. Lett.* **197**, 81 (1992).
10. Y. Gu, A. Widom, P. M. Champion, *J. Chem. Phys.* **100**, 2547 (1994).
11. D. Chernoff, R. M. Hochstrasser, A. Steele, *Proc. Natl. Acad. Sci. U.S.A.* **77**, 5606 (1980).
12. N. Agmon and J. J. Hopfield, *J. Chem. Phys.* **79**, 2042 (1983).
13. It should be noted that $\langle a(t) \rangle$ can affect the first moment of certain optical transitions (5), which evolve on the picosecond to nanosecond time scales [M. Lim, T. Jackson, P. Anfirrud, *Proc. Natl. Acad. Sci. U.S.A.* **90**, 5801 (1993)]. On the other hand, the quantity $\langle a(t) \rangle$ may have less effect on the resonance Raman intensity of the $\nu_{\text{Fe-His}}$ mode, which appears to be fully developed within a few picoseconds [S. Franzen *et al.*, *Struct. Biol.* **1**, 230 (1994)]. The more rapid development of the Raman intensity can be rationalized, if one postulates that the resonance Raman coupling of the Fe–His mode arises as a con-

sequence of reflection symmetry breaking in the d_{z^2} orbital, due to the (axial) histidine ligation, rather than as a result of the changes in iron out-of-plane displacement that occur as the system relaxes. However, as discussed by A. M. Ahmed *et al.* [*Chem. Phys.* **158**, 329 (1991)], the frequency of the Fe–His mode may well be affected by structural changes associated with the protein relaxation process.

14. The available evidence from x-ray crystallography of model compounds [W. R. Scheidt and P. Piciulo, *J. Am. Chem. Soc.* **98**, 1913 (1976)] suggests that the Fe–His bond is extended in the NO bound state, relative to the unbound species, as a result of additional electron density in the antibonding d_{z^2} orbital.
15. The factor of π arises under the condition $\tau_c \ll \tau_p$ because τ_p (~ 75 fs) corresponds to one-half of the Fe–His oscillatory period (~ 150 fs). A much smaller phase shift is expected for the low-frequency doming mode because τ_p is a much smaller fraction of its oscillatory period. The bound on τ_c ($\ll 75$ fs) is

somewhat shorter than (but not inconsistent with) that in previous studies, where the time scale for photodissociation was given as < 50 fs [J. Petrich, C. Poyart, J. L. Martin, *Biochemistry* **27**, 4049 (1988)], with the heme undergoing a major fraction of its initial out-of-plane displacement within the first 30 to 50 fs of photolysis [J. Petrich *et al.*, *ibid.* **30**, 3975 (1991)].

16. M. Walters and T. G. Spiro, *Biochemistry* **21**, 6989 (1982).
17. F. W. Wise, M. Rosker, G. Millhauser, C. L. Tang, *IEEE J. Quantum Electron.* **QE-23**, 1116 (1987).
18. X. Y. Li and M. Zgierski, *Chem. Phys. Lett.* **188**, 16 (1992).
19. Supported by National Science Foundation grant 94-05979 and National Institutes of Health grant AM-35090. We thank G. Millhauser for supplying us with the LPSVD algorithm and L. D. Ziegler for numerous helpful conversations.

24 June 1994; accepted 9 September 1994

February, and March 1991 reduced in amplitude by a factor of 2. This represents a weak tropical warming in the vicinity of the date line similar to that generally preceding a mature warm event.

All other boundary conditions—for example, ground wetness and snow depth—were treated as prognostic variables. All integrations used a CO_2 content of 330 parts per million. The monthly mean statistics for all the runs were generated by averaging the respective month over all years of integration. For example, the January mean for (i) would be the mean of 20 Januarys resulting from 20 years of integration.

The observed temperature anomalies averaged from December to May for the years 1982 to 1992 show regions of warming located over North America, Africa, Australia, northern Europe, and Asia (Fig. 1A) (8). Regions of cooling are located over Greenland, Mexico and the southwestern United States, northern India, and southeast Asia. The winter and spring period were chosen for the averaging because this was the period that shows warming as documented in the Intergovernmental Panel on Climate Change (IPCC) report (9). Globally, the AGCM-generated response in integration (ii) (Fig. 1B) closely resembles the observed anomalies. Although the match is not perfect, the comparison implies that the observed continental air temperature anomalies result from anomalous air-sea interactions because the only externally specified forcing in this simulation was the SSTs.

The main interannual climate variation associated with air-sea interactions is the El Niño–Southern Oscillation (ENSO) phenomenon. It is thus relevant to ask whether the observed global air temperature anomalies (Fig. 1A) are in response to this. To estimate the ENSO-related signal, we composited the observed air temperatures for those years between 1950 and 1993 when either major warm or cold events occurred. This period included a total of 18 events, nine of each sign. The air temperature anomalies for the cold ENSOs were almost everywhere of the opposite sign than those for the warm ENSOs. The structure of the composite anomaly, the average for the warm minus the cold ENSOs (Fig. 1C), is almost everywhere identical to that of Fig. 1A. The main discrepancies are the region around and poleward of 60°N in central Asia—where in contrast to Fig. 1A, the El Niño composite shows anomalies of opposite sign—and the northeast region of North America, which is not as cold. A similar compositing for integration (ii) indicates that the model response resembles the observed composite in Fig. 1C except (i) it is too strong in the tropical eastern hemisphere (10) and (ii), poleward of 70°N , it has temperatures that are too high. The anomaly

Simulations of Atmospheric Variability Induced by Sea Surface Temperatures and Implications for Global Warming

Arun Kumar,* Ants Leetmaa, Ming Ji

An atmospheric general circulation model was forced with observed interannual changes in the global sea surface temperatures (SSTs) for the period 1982 to 1993. The simulated seasonal surface air temperature patterns over land areas closely resemble the observed. Over most of the globe, the patterns also resemble those associated with El Niño events and are also reproduced in simulations with weak warm tropical SSTs near the date line. An exception is northern Asia, where the mechanisms for the observed warming are unclear. The results suggest that enhanced air-sea interactions resulting from recent, more persistent warm oceanic conditions in the tropics contributed to the observed global warming trend during this period.

Dominant interannual changes in the SST in the tropical Pacific Ocean are related to the quasi-periodic evolution of El Niño phenomena. These changes can have appreciable impact on the tropical and mid-latitude atmospheric temperatures (1). Although the impact of tropical SSTs on the tropical atmosphere has long been well simulated in atmospheric general circulation models (AGCMs) (2, 3), the impact on the mid-latitude atmospheric flows is only beginning to be realized (4, 5). Recent advances in the AGCMs have reached a stage where the impact of tropical SSTs on the global atmospheric flows can now be simulated.

To assess the capability of the National Meteorological Center (NMC) climate AGCM for seasonal prediction, we carried out several extended-range integrations forced with observed SSTs. This AGCM has a spectral triangular truncation at horizontal wave number 40 (T40) and has 18 levels in the vertical direction. The grid resolution of T40 is about 3° in latitude and longitude. It

is a lower resolution and differently tuned version of the AGCM used routinely at NMC for global short-range weather forecasts (6). We consider four model integrations. Integration (i) is 20-year integration with a climatological annual cycle of SSTs; the SSTs are an average of those observed for the period 1950 to 1980 (7). The atmospheric statistics resulting from this integration serve as the reference state from which anomalies in the other integrations are calculated. Model (ii) combines nine integrations all starting from 1 February 1982 with slightly different initial conditions and extending to 31 December 1993 in which the observed global SSTs (7) serve as the boundary conditions. Multiple runs are necessary to minimize the influence of atmospheric internal variability, which for a single run, can dominate the SST influence. Integration (iii) is a 20-year integration in which the global SST anomaly for the month of January 1992 was superimposed on the climatological annual cycle of SST used in (i). This represents conditions at the height of an El Niño. Integration (iv) is a 10-year integration similar to case (iii) but with SST anomalies as the mean of those for January,

National Meteorological Center, 5200 Auth Road, Camp Springs, MD 20746, USA.

*To whom correspondence should be addressed.